

Direction of actin flow dictates integrin LFA-1 orientation during leukocyte migration

Pontus Nordenfelt^{1,2,3,6,†}, Travis I. Moore^{1,3,†}, Shalin B. Mehta^{4,†}, Joseph Mathew Kalappurakkal^{1,2,5,#}, Vinay Swaminathan^{1,2,7,#}, Nobuyasu Koga^{8,9}, Talley J. Lambert¹⁰, David Baker⁸, Jennifer C. Waters¹⁰, Rudolf Oldenbourg⁴, Tomomi Tani⁴, Satyajit Mayor^{1,2,5,§}, Clare M. Waterman^{1,2,7,§} and Timothy A. Springer^{1,2,3,§,*}

1: Whitman Center, Marine Biological Laboratory, Woods Hole MA, USA

2: Physiology Course, Marine Biological Laboratory, Woods Hole MA, USA

3: Program in Cellular and Molecular Medicine, Children's Hospital, and Department of Biological Chemistry and Molecular Pharmacology and Medicine, Harvard Medical School, Boston MA, USA

4: Eugene Bell Center, Marine Biological Laboratory, Woods Hole MA, USA

5: National Center for Biological Sciences, Bangalore, IN

6: Current address: Division of Infection Medicine, Lund University, Lund, Sweden

7: Cell Biology and Physiology Center, NHLBI, NIH, Bethesda MD, USA

8: University of Washington, Seattle, WA and Howard Hughes Medical Institute

9: Current address: Institute for Molecular Science, Myodaiji, Okazaki, Japan

10: Department of Cell Biology, Harvard Medical School, Boston, MA, USA

†, #, §: Equal contribution

* Correspondence to:

Timothy A. Springer, Springer@crystal.harvard.edu

and Timothy.springer@childrens.harvard.edu

Integrin $\alpha\beta$ heterodimers mediate cell–cell and cell–matrix interactions and provide the traction for most cell migration in the body^{1,2}. Integrin ectodomains are unusually large and complex and assume three global conformational states (Fig. 1a) that differ up to 1,000-fold in affinity for ligand². Antigen recognition by lymphocytes as well as firm adhesion, diapedesis, and migration of leukocytes within tissues are dependent on lymphocyte function-associated antigen-1 (LFA-1), i.e. integrin $\alpha\text{L}\beta\text{2}$ or CD11a/CD18. Binding of LFA-1 to intercellular adhesion molecules (ICAMs) by the integrin head is communicated by 10 leg domains, through single-span transmembrane domains in each subunit, to the cytoskeleton via adaptors such as talins and kindlins³. How do integrins couple extracellular ligands to the actin cytoskeleton through a molecular mechanism that enables cell migration? Here, we test molecular predictions of a cytoskeletal force model of integrin activation⁴ in live cells. Using green fluorescent protein (GFP) inserted by fusing its N and C-termini to the LFA-1 head and polarization microscopy, we show that LFA-1 molecules engaged to ICAM-1 and the cytoskeleton are aligned and oriented relative to the direction of retrograde actin flow^{5,6} at the leading edge of migrating lymphocytes. Realistic 3D models of GFP-head fusions relate the transition dipole orientation of the GFP fluorophore^{7,8} to the orientation of engaged LFA-1 molecules on the cell surface. The orientation of the transition dipole in two distinct fusions correlates to the orientation of retrograde actin flow at the leading edge of migrating cells as measured by live-cell structured illumination microscopy. Alignment is dependent on cytoskeleton coupling to the β2 cytoplasmic tail and is consistent with integrins with a specific tilt being oriented in the same direction as retrograde actin flow. Together, these results strongly support the cytoskeletal force model of integrin activation and place the atomic structures of integrins in the context of cellular length-scale measurements that define how integrins orient as they function in leukocyte migration.

To report integrin orientation and dynamics on cell surfaces, we linked GFP into a loop of the β -propeller domain within the head of LFA-1 (Fig. 1a-d). We modeled with Rosetta any introduced linker residues, residues that vary in position in independent GFP structures, and residues in LFA-1 adjacent to the inserted GFP (Fig. 1d). A wide range of possible orientations of the two connections between GFP and LFA-1 was effectively sampled using polypeptide segments from the protein databank, selecting those that enabled connections at both the N and C-termini of GFP to be closed, and then minimizing the energy of the system with respect to the degrees of freedom of the connecting linkers⁹. The distribution of dipole orientations in the resulting ensembles (Fig. 1e) provides a range of orientations in which the actual orientation should be included, and also may approximate the contribution of GFP rotational motions to the decrease in emission anisotropy of GFP-LFA-1 fusions with the increase in length of the fusion segments (Extended Data Table 1). Three integrin-GFP fusions were studied with emission anisotropy total internal reflection fluorescence microscopy (EA-TIRFM)¹⁰ on the surface of live Jurkat T lymphoblasts migrating on ICAM-1 substrates (Fig. 1f, g). Emission anisotropy was highest for the truncated construct, α L-T; intermediate for the full length construct, α L-F; and lowest for the construct with linkers, α L-L, which had an emission anisotropy comparable to cytoplasmic GFP (Fig. 1g-h), consistent with the predicted GFP transition dipole alignment among members of structural ensembles obtained via Rosetta (Fig. 1e).

Fluorescence emission anisotropy (r) increases when the transition dipole of the GFP moiety attached to the integrin head is aligned with the excitation axis. Conversely, r decreases when the GFP transition dipole (and the integrin head to which it is attached) rotates in the time between excitation and emission. When whole cell or leading edge anisotropy is measured for multiple migrating cells that are randomly oriented with respect to the excitation axis, alignment effects are averaged out, and EA-TIRFM of GFP-integrin fusions may be used to measure the effect of integrin conformation on segmental motion of the integrin head (Fig. 1). Under basal conditions in our experiments, LFA-1 in the TIRF field adjacent to the substrate will be present in three conformational subpopulations: bent-closed, extended-closed, and extended-open (Fig. 1a). Extracellular Mn^{2+} , which activates integrin extension¹¹, strongly decreased α L-T emission anisotropy (Fig. 1g-h). Thus, shifting the conformational ensemble of integrins from bent-closed to extended-closed and extended-open conformations greatly increased integrin head segmental motion. This observation on integrins on cells is in excellent agreement with integrin crystal and EM structures that define the domain-domain junctions that are permissive of segmental motion and show that the head is markedly more flexible in the two extended conformations than in the bent conformation¹²⁻¹⁴.

We further examined the effects on α L-T emission anisotropy of expressing talin head domain fragment, which competes with talin binding to integrins but does not couple to actin¹⁵; and use of anti-CD43 as an integrin-independent substrate in place of ICAM-1¹⁶. Little change in average emission anisotropy was observed in either perturbation compared to α L-T on ICAM-1 (Fig. 1g and h), consistent with little redistribution among the three states in the integrin conformational ensemble. On ICAM-1 substrates, much of the LFA-1 is not engaged and is present in the bent conformation¹⁷. This observation predicts that inhibiting integrin engagement with anti-CD43, or inhibiting stabilization of the high affinity state with talin head overexpression, would have little overall effect on the partition of LFA-1 among its three conformational states, in agreement with the emission anisotropy results.

Compared to an extended, unengaged integrin, an extended, engaged integrin is predicted to have its head motion dampened by attachment to and alignment by the actin cytoskeleton and the substrate-bound ligand. Whole cell images showed that anisotropy was higher in edge regions than non-edge regions for α L-T and α L-F (Fig. 1g), suggesting more engagement in leading edges. To further test this hypothesis, we compared the ratio of top anisotropy values ($> \text{mean} + 1 \text{ s.d.}$ or $\sim 16\%$ of pixels) in leading edge regions to non-edge regions (Fig. 1j). Indeed, this ratio was significantly higher for α L-T and α L-F than α L-L or GFP (Fig. 1j). Furthermore, the ratio of leading/non-edge α L-T emission anisotropy was significantly reduced by overexpressing talin head or using anti-CD43 substrates, suggesting that these conditions decreased the ratio of engaged LFA-1 in leading edge compared to non-edge regions.

We next measured angular dependence of the GFP anisotropy using EA-TIRFM to test the hypothesis that integrin engagement to an immobilized ligand and the cytoskeleton would cause the integrin and its associated GFP transition dipole to adopt a specific orientation relative to the direction of actin retrograde flow (Figs. 2, 3). Flow is normal to the leading edge of migrating cells (Fig. 1c) as shown below in Fig. 3. We tested for the angular \cos^2 dependence of fluorescence anisotropy with respect to the orientation of the leading edge relative to the axis of polarized excitation in EA-TIRFM (Fig. 2a)^{18,19}. Cells in movies were segmented into whole cell, edge and protruding regions, and finally within the leading edge (lamellipodium) (Fig. 2b-c, steps 1-4). Geometric shape-based orientation was determined by the angle from the cell edge to mid-region (Fig. 2b, see Methods), making it possible to test for angular dependence of anisotropy within each cell. For α L-T, angular dependence of emission anisotropy with respect to the leading edge in the cell protrusion fit the \cos^2 function (Fig. 2a). The amplitude (A) which signifies the extent of modulation, increased towards the leading edge (Fig. 2d, see also Extended Data Fig 1-4, Extended Data Table 2 and Movie 1). The phase shift of the maximum anisotropy of the integrin-GFP chimera relative to the angle between the membrane normal and the excitation axis in segmented leading edges, θ_d , was $98.5^\circ \pm 37.6^\circ$ for α L-T and $75.7^\circ \pm 46.6^\circ$ (mean \pm std) for α L-F. Compared to the integrin-GFP fusions, anisotropy and amplitudes were lower and fits were poor with cytosolic GFP and membrane-bound GFP (CAAX) (Fig. 2d-e, Movie 2). Perturbation of α L-T interactions with Mn^{2+} , expression of talin head domain, or the non-integrin substrate anti-CD43 lowered amplitude, indicative of a loss of integrin alignment (Fig. 2e). These results show that LFA-1 becomes oriented in the lamellipodium relative to the adjacent leading edge, that this alignment is disrupted by dysregulation of LFA-1 adhesiveness by Mn^{2+} , and that alignment is dependent on ICAM-1 engagement and talin linkage to the actin cytoskeleton.

Actin flow is known to be retrograde and normal to the leading edge in migrating fibroblasts and epithelial cells²⁰⁻²² and within the immunological synapse in non-migrating T cells²³. We defined actin dynamics in migrating T cells expressing lifeact-mNeonGreen using the super-resolution capabilities of structured illumination microscopy (SIM). Migrating T cells lacked organized actin stress fibers characteristic of most non-muscle cells (Fig. 3a). Optical flow analysis of time-lapse movies (Fig. 3b)^{24,25} showed that flow was retrograde at close to 90° relative to the leading edge (Fig. 3c) and was rapid at $17 \pm 1 \text{ nm/s}$ on ICAM-1 substrates (Fig. 3d, Movie 3) as confirmed with kymographs (Extended Data Fig. 6). On anti-CD43 substrates, flow was significantly faster ($71 \pm 4 \text{ nm/sec}$, Movie 4) while flow on mixed ICAM-1 and anti-CD43 substrates was intermediate in velocity ($34 \pm 2 \text{ nm/sec}$) (Fig. 3c, Movie 5). The ability of ICAM-1 on substrates to slow retrograde actin flow, and the intermediate results with mixed anti-CD43 and ICAM-1 substrates, strongly suggest that LFA-1 is mechanically linked to the actin in

retrograde flow. Although indirect regulatory mechanisms cannot be ruled out, the most straightforward interpretation is that flowing actin is slowed by the linkage of LFA-1 to both the actin cytoskeleton inside the cell and ICAM-1 on the substrate. Linkage of engaged LFA-1 to a force-producing actin network is similar to that proposed in the molecular clutch model of mesenchymal cell migration^{26,27}. This tensile force would be exerted by the actin cytoskeleton along the direction of actin flow and lead to the alignment of LFA-1 demonstrated with EA-TIRFM. Force exertion provides a mechanism for alignment of the GFP-LFA-1 transition dipole, and is in keeping with the observation that alignment of the emission dipole with respect to the membrane normal is disrupted by talin head (Fig. 2e), which disrupts linkage of integrins to the actin cytoskeleton.

We further tested the role of the actin cytoskeleton in integrin alignment by disrupting two prominent drivers of actin flow, contractility and polymerization. Blebbistatin, an inhibitor of myosin-dependent actin filament contractility, had no effect on α L-T anisotropy (Fig. 3e-f, Extended Data Fig. 5), consistent with lack in T cells of actin stress fibers. In contrast, cytochalasin D, an inhibitor of actin polymerization, significantly decreased LFA-1 anisotropy (Fig. 3e-f). Together, these results show that an intact cytoskeleton is required for LFA-1 anisotropy and suggest that actin polymerization, a mechanism operative in the lamellipodium to generate retrograde flow that is independent of actomyosin contraction²⁰, is required for LFA-1 anisotropy and hence alignment. Altogether, the alignment of the transition dipole in LFA-1 GFP fusions, the studies with inhibitors, and measurements of actin retrograde flow direction and velocity on different substrates, suggest that actin retrograde flow at the leading edge builds up molecular ordering and alignment of LFA-1 engaged with an ICAM-coated surface.

In an independent microscopy technique, instantaneous FluoPolScope²⁸, fluorophore dipoles in GFP-LFA-1 were excited isotropically with circular polarized laser TIRF excitation, and the emission was split four ways using polarization beam splitters and simultaneously projected onto four quadrants of a single CCD detector (Fig. 4a). Orientation and polarization factor p (analogous to anisotropy r) information about the GFP-LFA-1 emission dipole ensemble present in each pixel weighted by intensity in migrating T cells was averaged over multiple leading edge and cell body segments (Fig. 4b-d). α L-T emission polarization at leading edges was significantly higher than for α L-F and also higher than for α L-T in the cell body or for GFP in solution or in the cytoplasm (Fig. 4c). Leading edge emission polarization factor on ICAM-1 substrates was significantly decreased by extracellular Mn^{2+} and on anti-CD43 substrates (Fig. 4c). These polarization factor results were in excellent agreement with the anisotropy results obtained by EA-TIRFM.

Because FluoPolScope measures emission dipole orientation in each pixel, it enables absolute measurements of orientation. Whereas emission dipole orientation in a representative cell (Fig. 4e) has an angular dependence in the microscope frame of reference (Fig. 4f), emission dipole orientation collapses to a narrow distribution relative to the membrane normal (Fig. 4d, g). Emission dipole orientation relative to membrane normal (θ_d) over 264-351 segments from 21-31 cells (mean \pm s.d.) was $95.4^\circ \pm 10.1^\circ$ for α L-T and $71.7^\circ \pm 17.9^\circ$ for α L-F (Fig. 4d). These values are within 4° of those from EA-TIRFM, but have much smaller errors, likely because phase shift calculations in EA-TIRFM were dependent on sampling a wide range of leading edge

orientations and showed more cell to cell variation. Circular Gaussians also fit the FluoPolScope data well (propeller-shaped outlines in Fig. 4d).

To estimate the orientation of the aligned LFA-1, we used α L-T-GFP. Rosetta predicts for α L-T-GFP a narrower range of dipole orientations and higher polarization factor than for α L-F-GFP (Fig. 1e and Extended Data Fig. 8-10), in agreement with its higher value of experimentally measured polarization factor (Fig. 4d). Defining molecular orientation on the cell surface required constructing a frame of reference that places integrin atomic coordinates in microscope coordinates (Fig. 4h). The xy plane was defined as parallel to the microscope TIRF field, where x represents the direction of lamellipodial movement. Three atoms conserved in position among integrin heterodimer complexes with ligands and among conformational states defined the xz plane (Fig. 4h). Integrin orientation relative to the reference frame was expressed in spherical coordinates. Both integrin head rotation θ in the xy plane and tilt ϕ relative to the z axis will affect the measured projection of the GFP transition dipole in the xy plane (Fig. 4j). The experimentally determined value of $\theta_d = 95.4 \pm 10.1^\circ$ for α L-T is in perfect agreement with $\theta = 0^\circ$, as predicted by alignment by retrograde actin flow, and $\phi = 45^\circ$ (Fig. 4j). The range of tilts (variation in ϕ) explored in Fig. 4j shows that ϕ values of 67.5° and 22.5° are also compatible with the experimentally determined θ_d value when combined with θ values in the integrin reference frame of 10° and -10° , respectively (Fig. 4j). We conclude that we can define the orientation of engaged LFA-1 on cell surfaces with respect to the reference frame as within about 10° of $\theta = 0$ and within about 25° of $\phi = 45^\circ$. The orientation predicted by α L-F-GFP is similar, but less well defined (Extended Data Fig 9). The transition dipole orientation we measure is compatible with an integrin orientation of either $\theta = 0^\circ$ or 180° ; however, evidence that the cytoskeleton applies the force to the integrin β -subunit forces us to choose β retrograde of α , which is fulfilled only by $\theta = 0^\circ$.

We therefore conclude that on the surface of a migrating T cell, cytoskeletal force causes the LFA-1 head to align to the direction of actin flow, and to tilt relative to the membrane normal (Fig. 4i-l). The integrin β -leg and ICAM-1 have flexible inter-domain junctions and the α I domain is flexibly linked to the β I domain and β -propeller domain²⁹. Force balance requires that tensile force applied results in the straightening of the flexible domain-domain linkages in this force-bearing chain like links in a tow-chain, and aligns them in the direction of force. Thus our measurements not only reveal the orientation of the integrin head near the center of this chain, but also suggest that the entire chain has an orientation similar to the path that force takes through the β I domain in the integrin head (Fig. 4i and 4l).

Little has been known about cell surface receptors built from multiple tandem extracellular domains linked to single-span transmembrane domains with respect to their orientation in the plasma membrane. Furthermore, it has been difficult to relate conformational states of isolated receptor glycoproteins to their conformation, function, and orientation on cell surfaces. Here, we have found that the emission anisotropy of the GFP-tagged head of LFA-1 correlates with transition between bent and extended states, and between free and engaged extended states. We have demonstrated that integrin LFA-1 becomes aligned at the leading edge of migrating T cells, that integrin alignment correlates with actin flow alignment, that the orientation of the integrin resembles that predicted by application of force by the actin cytoskeleton to the integrin β -subunit (Fig. 4k), and that agents that disrupt LFA-1 linkage to the cytoskeleton or that artificially activate LFA-1 disrupt LFA-1 alignment. Tensile force transmitted through integrins stabilizes

their most extended state, which is also their highest affinity state, and thereby provides a simple and elegant mechanism for coordinating cytoskeletal activity inside the cell with binding to extracellular ligands in cell migration⁴. The same mechanism also provides the simplest explanation for alignment of integrins with the direction of actin retrograde flow. Our results place molecular understanding of integrin structure and function within the context of integrin function in cell migration and in linking the extracellular environment to the actin cytoskeleton. Results here for an integrin that recognizes ICAMs, contains an αI domain, is not found in focal adhesions, and links to rapid actin retrograde flow and cell migration, are similar to those in a companion paper for an integrin that recognizes fibronectin, lacks an αI domain, is found in focal adhesions, and is linked to slow actin stress fiber retrograde flow and slow migration (Swaminathan et al., co-submitted MS). Since 22 of the 24 mammalian integrin $\alpha\beta$ heterodimers have β -subunits that link to the actin cytoskeleton, these findings are expected to be of wide relevance.

Acknowledgements

We thank Nikon Instruments and Andor Technology for use of imaging equipment, Thomas Holder at Schrodinger for Pymol/Python scripts and advice to create cgo representations of ellipsoids, torus, and dipoles, and Einat Schnur, Gabriel Billings and Amy Gladfelter for help, advice and discussion. Supported by the Lillie Research award from Marine Biological Laboratory and the University of Chicago (CMW, TAS, SM, TT), NIH 5R13GM085967 grant to the Physiology Course at Marine Biological Laboratory, HHMI Summer Institute at Marine Biological Laboratory (SM), NIH CA31798 (TAS, PN, TJM), NIH GM100160 (TT, SM), NIH GM092802 (DB, NK), NIH GM114274 (RO, SM) National Center for Biological Sciences-Tata Institute of Fundamental Research (SM, JMK), JC Bose Fellowship and HFSP Grant RGP0027/2012 (SM), NHLBI Division of Intramural Research (CMW, VS), Swedish Research Council VR 524-2011-891 Fellowship (PN), Swedish Society for Medical Research SSMF Fellowship (PN).

Author contributions

This project was initiated at the Woods Hole Physiology Course. PN, TIM, SM, CMW and TAS designed the research. TT, SM, CMW, RO, and TAS supervised the project. PN designed and made the GFP-integrin constructs. TIM performed imaging experiments and analyzed data. PN wrote image processing and analysis code and analyzed data. SBM and JMK set up polarisation microscopes and RO advised on analysis. NK, TAS, and DB performed Rosetta modeling. TAS constructed the integrin-microscope reference frame and defined the GFP transition dipole orientation within Rosetta models. TAS and SBM analyzed Rosetta data. TIM, TJL, and JCW performed SIM experiments and analysis. SBM, JMK and VS contributed to image data analysis. PN, TIM, and TAS drafted the manuscript. All authors discussed the results and commented on the manuscript.

References

- 1 Hynes, R. O. Integrins: bidirectional, allosteric signaling machines. *Cell* **110**, 673-687 (2002).
- 2 Springer, T. A. & Dustin, M. L. Integrin inside-out signaling and the immunological synapse. *Curr. Opin. Cell Biol.* **24**, 107-115, doi:10.1016/j.ceb.2011.10.004 (2012).
- 3 Calderwood, D. A., Campbell, I. D. & Critchley, D. R. Talins and kindlins: partners in integrin-mediated adhesion. *Nat. Rev. Mol. Cell Biol.* **14**, 503-517, doi:10.1038/nrm3624 (2013).
- 4 Zhu, J. *et al.* Structure of a complete integrin ectodomain in a physiologic resting state and activation and deactivation by applied forces. *Mol. Cell* **32**, 849-861 (2008).
- 5 Gardel, M. L., Schneider, I. C., Aratyn-Schaus, Y. & Waterman, C. M. Mechanical integration of actin and adhesion dynamics in cell migration. *Annu. Rev. Cell Dev. Biol.* **26**, 315-333, doi:10.1146/annurev.cellbio.011209.122036 (2010).
- 6 Renkawitz, J. *et al.* Adaptive force transmission in amoeboid cell migration. *Nat. Cell Biol.* **11**, 1438-1443, doi:10.1038/ncb1992 (2009).
- 7 Rosell, F. I. & Boxer, S. G. Polarized absorption spectra of green fluorescent protein single crystals: transition dipole moment directions. *Biochemistry* **42**, 177-183, doi:10.1021/bi0266535 (2003).
- 8 Shi, X. *et al.* Anomalous negative fluorescence anisotropy in yellow fluorescent protein (YFP 10C): quantitative analysis of FRET in YFP dimers. *Biochemistry* **46**, 14403-14417, doi:10.1021/bi701575n (2007).
- 9 Huang, P. S. *et al.* RosettaRemodel: a generalized framework for flexible backbone protein design. *PLoS One* **6**, e24109, doi:10.1371/journal.pone.0024109 PONE-D-11-09414 [pii] (2011).
- 10 Ghosh, S., Saha, S., Goswami, D., Bilgrami, S. & Mayor, S. Dynamic imaging of homo-FRET in live cells by fluorescence anisotropy microscopy. *Methods Enzymol.* **505**, 291-327, doi:10.1016/B978-0-12-388448-0.00024-3 (2012).
- 11 Takagi, J., Petre, B. M., Walz, T. & Springer, T. A. Global conformational rearrangements in integrin extracellular domains in outside-in and inside-out signaling. *Cell* **110**, 599-611 (2002).
- 12 Xie, C. *et al.* Structure of an integrin with an α I domain, complement receptor type 4. *EMBO J.* **29**, 666-679 (2010).
- 13 Nishida, N. *et al.* Activation of leukocyte β 2 integrins by conversion from bent to extended conformations. *Immunity* **25**, 583-594 (2006).

- 14 Zhu, J. *et al.* The structure of a receptor with two associating transmembrane domains on the cell surface: integrin $\alpha_{Ib}\beta_3$. *Mol. Cell* **34**, 234-249 (2009).
- 15 Calderwood, D. A. *et al.* The talin head domain binds to integrin β subunit cytoplasmic tails and regulates integrin activation. *J. Biol. Chem.* **274**, 28071-28074 (1999).
- 16 Nguyen, K., Sylvain, N. R. & Bunnell, S. C. T cell costimulation via the integrin VLA-4 inhibits the actin-dependent centralization of signaling microclusters containing the adaptor SLP-76. *Immunity* **28**, 810-821, doi:10.1016/j.immuni.2008.04.019 (2008).
- 17 Smith, A. *et al.* A talin-dependent LFA-1 focal zone is formed by rapidly migrating T lymphocytes. *J. Cell Biol.* **170**, 141-151 (2005).
- 18 Kampmann, M., Atkinson, C. E., Mattheyses, A. L. & Simon, S. M. Mapping the orientation of nuclear pore proteins in living cells with polarized fluorescence microscopy. *Nature Publishing Group* **18**, 643-649, doi:10.1038/nsmb.2056 (2011).
- 19 Vrabioiu, A. M. & Mitchison, T. J. Structural insights into yeast septin organization from polarized fluorescence microscopy. *Nature* **443**, 466-469, doi:10.1038/nature05109 (2006).
- 20 Ponti, A., Machacek, M., Gupton, S. L., Waterman-Storer, C. M. & Danuser, G. Two distinct actin networks drive the protrusion of migrating cells. *Science* **305**, 1782-1786, doi:10.1126/science.1100533 305/5691/1782 [pii] (2004).
- 21 Gardel, M. L. *et al.* Traction stress in focal adhesions correlates biphasically with actin retrograde flow speed. *J. Cell Biol.* **183**, 999-1005, doi:10.1083/jcb.200810060 (2008).
- 22 Thievesten, I. *et al.* Vinculin-actin interaction couples actin retrograde flow to focal adhesions, but is dispensable for focal adhesion growth. *J. Cell Biol.* **202**, 163-177, doi:10.1083/jcb.201303129 (2013).
- 23 Comrie, W. A. & Burkhardt, J. K. Action and Traction: Cytoskeletal Control of Receptor Triggering at the Immunological Synapse. *Front Immunol.* **7** (2016).
- 24 Abramoff, M. D., Niessen, W. J. & Viergever, M. A. Objective quantification of the motion of soft tissues in the orbit. *IEEE Trans. Med. Imaging* **19**, 986-995, doi:10.1109/42.887614 (2000).
- 25 Lucas, B. D. & Kanade, T. in *Proceedings of the 7th international joint conference on Artificial intelligence - Volume 2* 674-679 (Morgan Kaufmann Publishers Inc., Vancouver, BC, Canada, 1981).
- 26 Gupton, S. L. & Waterman-Storer, C. M. Spatiotemporal feedback between actomyosin and focal-adhesion systems optimizes rapid cell migration. *Cell* **125**, 1361-1374, doi:S0092-8674(06)00719-7 [pii] 10.1016/j.cell.2006.05.029 (2006).

- 27 Case, L. B. & Waterman, C. M. Integration of actin dynamics and cell adhesion by a three-dimensional, mechanosensitive molecular clutch. *Nat. Cell Biol.* **17**, 955-963, doi:10.1038/ncb3191 (2015).
- 28 Mehta, S. B. *et al.* Dissection of molecular assembly dynamics by tracking orientation and position of single molecules in live cells. *Proc Natl Acad Sci U S A.* (2016).
- 29 Sen, M., Yuki, K. & Springer, T. A. An internal ligand-bound, metastable state of a leukocyte integrin, $\alpha_x\beta_2$. *J. Cell Biol.* **203**, 629-642, doi:10.1083/jcb.201308083 (2013).
- 30 Fourkas, J. T. Rapid determination of the three-dimensional orientation of single molecules. *Optics letters* **26**, 211-213 (2001).
- 31 Anthis, N. J. *et al.* The structure of an integrin/talin complex reveals the basis of inside-out signal transduction. *EMBO J.* **28**, 3623-3632, doi:10.1038/emboj.2009.287 (2009).
- 32 Recacha, R. *et al.* Crystal structures of an ICAM-5 ectodomain fragment show electrostatic-based homophilic adhesions. *Acta Crystallogr. D Biol. Crystallogr.* **70**, 1934-1943, doi:10.1107/S1399004714009468 (2014).
- 33 Casasnovas, J. M., Springer, T. A., Liu, J.-H., Harrison, S. C. & Wang, J.-H. The crystal structure of ICAM-2 reveals a distinctive integrin recognition surface. *Nature* **387**, 312-315 (1997).
- 34 Shimaoka, M. *et al.* Structures of the α_L I domain and its complex with ICAM-1 reveal a shape-shifting pathway for integrin regulation. *Cell* **112**, 99-111 (2003).
- 35 Sen, M. & Springer, T. A. Leukocyte integrin $\alpha_L\beta_2$ headpiece structures: The α_L domain, the pocket for the internal ligand, and concerted movements of its loops. *Proc Natl Acad Sci U S A.* **113**, 2940-2945 (2016).

Figure Legends

Figure 1. GFP-LFA-1 fusions, emission anisotropy, and integrin head segmental motion.

- a. Three global conformational states of integrins². Cartoons depict each integrin domain and GFP with its transition dipole (red double-headed arrows).
 - b. Ribbon diagram of the integrin headpiece of α L-T. The GFP insertion site in the β -propeller domain is arrowed.
 - c. Cartoon as in (a) of ICAM-engaged, extended-open LFA-1 showing direction of leading edge motion and actin flow. Large arrows show pull on integrin- β by actin and resistance by ICAM-1. Axes shown in (a) and (c) are similar to those in the references state in Fig. 4.
 - d. Sequences and boundaries used in GFP-LFA-1 fusions. Highlighted residues were modeled by Rosetta to link GFP to the integrin (yellow) and altered in backbone and sidechain orientation to minimize energy (yellow and orange).
 - e. Orientation of the transition dipole in GFP-LFA-1 fusions. Integrin domains are shown as ellipsoids or torus and GFP is shown in cartoon for 1 ensemble member. GFP transition dipoles are shown as cylinders with cones at each end for 20 representative Rosetta ensemble members, with the asymmetry of GFP referenced by using different colors for the ends of transition dipoles.
 - f. Emission anisotropy TIRF Microscopy.
 - g. Representative images from movies of Jurkat T cells stably expressing GFP-LFA-1 fusions migrating on ICAM-1 (left) or showing for α L-T the effects of 1 mM Mn^{2+} , co-expression of talin head domain, or migration on anti-CD43 (right). Each pair of panels shows total GFP fluorescence intensity (left) and anisotropy (right, color scale bar to right). Scale bars are 5 μ m.
 - h-j. Emission anisotropy of GFP-LFA-1 fusions, averaged over Jurkat T cells migrating in random directions, in at least five independent experiments.
 - h. Anisotropy averaged over multiple whole cells.
 - i. Example of cell segmentation into leading edge and non-edge portions of α L-F with total fluorescence (left) and anisotropy (right three panels with color scale bar to left).
 - j. Ratio of high anisotropy (r) in leading edge compared to non-edge regions per cell (mean \pm sd) using the r values of pixels in each region > 1 sd above mean r . Box plots in h and j show the full range (whiskers) of observations with median as line and 25-75 percentile range boxed. Kruskal-Wallis test with multiple comparison correction gave the indicated p-values. N (number of cells) for α L-T was 37 (h) and 30 (j) and ranged from 9 to 52 for other groups.
- *: $p < 0.05$; **: $p < 0.01$; ****: $p < 0.0001$.

Figure 2 – Orientation of LFA-1 in the leading edge of migrating cells by EA-TIRFM.

- a. Schematic showing relation between excitation polarization, transition dipole orientation, and emission anisotropy in EA-TIRFM.
- b-c. Representative segmentation for a migrating Jurkat T cell expressing α L-T-GFP with corresponding maps of orientation relative to the cell midline (b) and anisotropy, r , (c) in the segmented regions (1-4). Scale bar = 5 μ m.
- d. Emission anisotropy of segmented leading edge regions for α L-T, cytosolic GFP, and GFP-CAAX (Extended Data Figs. 1 and 4). Scatter plots show anisotropy vs orientation relative to the cell midline for each pixel in individual, representative cells (from b and c for α L-T), the

running average (blue) and fit to the equation in panel a (red). Values for the fit parameters (A = absolute amplitude, θ_d = phase shift, R^2 = goodness-of-fit) are displayed in each plot. e. Absolute amplitudes of emission anisotropy fits to the \cos^2 relationship. Box plots are as in Fig. 1, with whiskers showing the 5-95 percentile range. Kruskal-Wallis test with multiple comparison correction to aL-T leading edge data ($N=206$) gave p-values from left to right: <0.0001 ($N=85$); <0.0001 ($N=52$); <0.0001 ($N=58$); 0.0033 ($N=185$); <0.0001 ($N=71$); <0.0001 ($N=83$); <0.0001 ($N=55$) with N leading edges. See Extended Data Table 2 for more details. A two-tailed Mann-Whitney test of aL-F in absence and presence of talin head gave a p-value of 0.0059. ** $p < 0.01$, **** $p < 0.0001$.

Figure 3 – Actin flow dynamics, orientation, and relation to GFP-LFA-1 anisotropy in migrating T cells

- Representative frames of structured illumination microscopy movies (above) of the actin cytoskeleton visualized with lifeact-mNeonGreen in Jurkat T cells migrating on ICAM-1 (10 $\mu\text{g/ml}$), anti-CD43 IgG (10 $\mu\text{g/ml}$), or their mixture (10 $\mu\text{g/ml}$ each). Optical actin flow vector maps of the same cells (below) with zoom insets. Vectors encode flow direction by color (circular keys in the direction from center of circle to perimeter) and velocity by length. Scale bars encode dimensions in the micrograph (upper, 5 μm) and velocity (lower, 30 nm/s).
- Actin flow direction relative to tangent of leading edge membrane. Bins of 15° are shown with gaussian fit and mean \pm SEM. ICAM-1, $N=62$; αCD43 , $N=63$; ICAM-1+ αCD43 , $N=67$.
- Leading edge actin flow velocity from optical flow analysis. Plots show full range of the data. Bars show mean \pm SD. Two-tailed Mann-Whitney tests all show $p < 0.0001$ (****). Number of cells (N) were ICAM-1, 39; αCD43 , 38; and ICAM-1+anti-CD43, 25.
- Whole cell emission anisotropy in Jurkat T cells treated as in e. Mann-Whitney test for DMSO ($N = 37$) vs blebbistatin ($N = 9$) was 0.130 and for DMSO vs cytochalasin D ($N = 14$) was 0.003. ** $p < 0.01$.
- Representative total fluorescence intensity ($I_{||} + 2I_{\perp}$, top) and anisotropy (bottom) of fixed Jurkat T cells migrating on ICAM-1 (10 $\mu\text{g/ml}$) expressing aL-T-GFP treated with DMSO as control, blebbistatin (100 μM), or cytochalasin D (100 nM). Scale bars: 5 μm .

Figure 4 – Integrin head segmental motion and orientation along the axis of actin retrograde flow in migrating T cells measured by instantaneous FluoPolScope.

- Schematic of Instantaneous FluoPolScope.
- Representative total fluorescence intensity ($I_{||} + 2I_{\perp}$) image of $\alpha\text{L-T}$ Jurkat T cell migrating on ICAM-1 (10 $\mu\text{g/ml}$) with overlay of segments (white = leading edge, magenta = cell body), normal to leading edge tangent (yellow), and average GFP emission dipole orientation with length proportional to polarization factor (red). Scale bars = 1 μm . Panel below is enlarged from dashed area.
- Polarization factor of T cells migrating in random directions. Box plots show the full range (whiskers) of observations with median as line and 25-75 percentile range boxed. Kruskal-Wallis test with multiple comparison correction of leading edges gave the indicated p-values to $\alpha\text{L-T}$ using N number of cells shown in panel d. ** $p < 0.01$, *** $p < 0.001$, **** $p < 0.0001$.
- Radial histograms of GFP transition dipole projection in image plane relative to the membrane normal (θ_d). Each histogram wedge shows mean intensity-weighted polarization factor (p) in 15°

bins (solid outlines) and is reflected to represent the dyad symmetry axis of the dipole. Dashed propeller-shaped outlines in the lower two panels show the fit of the data to a circular Gaussian. e-g. e. A representative aL-T Jurkat cell migrating on ICAM-1 was segmented as shown in (b). Segments are color coded in blue-red rainbow around the leading edge and are shown in same color in f and g. Each segment is represented as a reflected wedge in f and g at the angle of its emission dipole projection with respect to the microscope (f) or with respect to the membrane normal (θ_d) (g).

h-i. Integrin-microscope reference frame. xy and xz planes are black and blue grids, respectively. Ca atoms used to define the origin (red), x axis (gold), and xz plane (silver) are shown as large spheres. The GFP transition dipole (red) and its projection on the image plane (yellow-orange) are shown as cylinders with cones at each end. A spherical coordinate radial marker r (red arrow) is used to compare integrin orientations between h and i.

h. The reference state with $\theta = 0^\circ$ and $\phi = 90^\circ$.

i. The integrin orientation with $\theta = 0^\circ$ and $\phi = 45^\circ$ that fits data well.

j. The image plane with dipole positions of Rosetta ensemble members (lowest 40% in energy) projected from a spherical surface and shown as open grey circles. Projections are all in the reference frame with $\theta = 0^\circ$ and with tilts in ϕ from 67.5° to 11.25° . Silver, red, and gold circles show the same integrin reference atoms as in h & i. The calculated ensemble transition dipole³⁰ is projected as a green line with length proportional to p . The transition dipole orientation determined by FluoPolScope is shown as black line with ± 1 s.d. shown as dashed lines.

k. Schematic showing integrin and GFP dipole orientation relative to tensile force between the actin cytoskeleton and ICAM (arrows) in migrating cells. See Fig. 1a and c for key to domain color code.

l. Model of cytoskeletal force acting on an integrin drawn to scale tilted at $\phi = 45^\circ$.

Structures^{4,14,29,31-35} were assembled and rotated at domain-domain junctions known to be flexible and depicted with PyMol.

a Bent-closed Extended-closed Extended-open with force Cytoskeleton

b β -propeller α 416-417 α 1 β 1 β 2 β 3 β 4 β 5 β 6 β 7 β 8 β 9 β 10 β 11 β 12 β 13 β 14 β 15 β 16 β 17 β 18 β 19 β 20 β 21 β 22 β 23 β 24 β 25 β 26 β 27 β 28 β 29 β 30 β 31 β 32 β 33 β 34 β 35 β 36 β 37 β 38 β 39 β 40 β 41 β 42 β 43 β 44 β 45 β 46 β 47 β 48 β 49 β 50 β 51 β 52 β 53 β 54 β 55 β 56 β 57 β 58 β 59 β 60 β 61 β 62 β 63 β 64 β 65 β 66 β 67 β 68 β 69 β 70 β 71 β 72 β 73 β 74 β 75 β 76 β 77 β 78 β 79 β 80 β 81 β 82 β 83 β 84 β 85 β 86 β 87 β 88 β 89 β 90 β 91 β 92 β 93 β 94 β 95 β 96 β 97 β 98 β 99 β 100 β 101 β 102 β 103 β 104 β 105 β 106 β 107 β 108 β 109 β 110 β 111 β 112 β 113 β 114 β 115 β 116 β 117 β 118 β 119 β 120 β 121 β 122 β 123 β 124 β 125 β 126 β 127 β 128 β 129 β 130 β 131 β 132 β 133 β 134 β 135 β 136 β 137 β 138 β 139 β 140 β 141 β 142 β 143 β 144 β 145 β 146 β 147 β 148 β 149 β 150 β 151 β 152 β 153 β 154 β 155 β 156 β 157 β 158 β 159 β 160 β 161 β 162 β 163 β 164 β 165 β 166 β 167 β 168 β 169 β 170 β 171 β 172 β 173 β 174 β 175 β 176 β 177 β 178 β 179 β 180 β 181 β 182 β 183 β 184 β 185 β 186 β 187 β 188 β 189 β 190 β 191 β 192 β 193 β 194 β 195 β 196 β 197 β 198 β 199 β 200 β 201 β 202 β 203 β 204 β 205 β 206 β 207 β 208 β 209 β 210 β 211 β 212 β 213 β 214 β 215 β 216 β 217 β 218 β 219 β 220 β 221 β 222 β 223 β 224 β 225 β 226 β 227 β 228 β 229 β 230 β 231 β 232 β 233 β 234 β 235 β 236 β 237 β 238 β 239 β 240 β 241 β 242 β 243 β 244 β 245 β 246 β 247 β 248 β 249 β 250 β 251 β 252 β 253 β 254 β 255 β 256 β 257 β 258 β 259 β 260 β 261 β 262 β 263 β 264 β 265 β 266 β 267 β 268 β 269 β 270 β 271 β 272 β 273 β 274 β 275 β 276 β 277 β 278 β 279 β 280 β 281 β 282 β 283 β 284 β 285 β 286 β 287 β 288 β 289 β 290 β 291 β 292 β 293 β 294 β 295 β 296 β 297 β 298 β 299 β 300 β 301 β 302 β 303 β 304 β 305 β 306 β 307 β 308 β 309 β 310 β 311 β 312 β 313 β 314 β 315 β 316 β 317 β 318 β 319 β 320 β 321 β 322 β 323 β 324 β 325 β 326 β 327 β 328 β 329 β 330 β 331 β 332 β 333 β 334 β 335 β 336 β 337 β 338 β 339 β 340 β 341 β 342 β 343 β 344 β 345 β 346 β 347 β 348 β 349 β 350 β 351 β 352 β 353 β 354 β 355 β 356 β 357 β 358 β 359 β 360 β 361 β 362 β 363 β 364 β 365 β 366 β 367 β 368 β 369 β 370 β 371 β 372 β 373 β 374 β 375 β 376 β 377 β 378 β 379 β 380 β 381 β 382 β 383 β 384 β 385 β 386 β 387 β 388 β 389 β 390 β 391 β 392 β 393 β 394 β 395 β 396 β 397 β 398 β 399 β 400 β 401 β 402 β 403 β 404 β 405 β 406 β 407 β 408 β 409 β 410 β 411 $\$

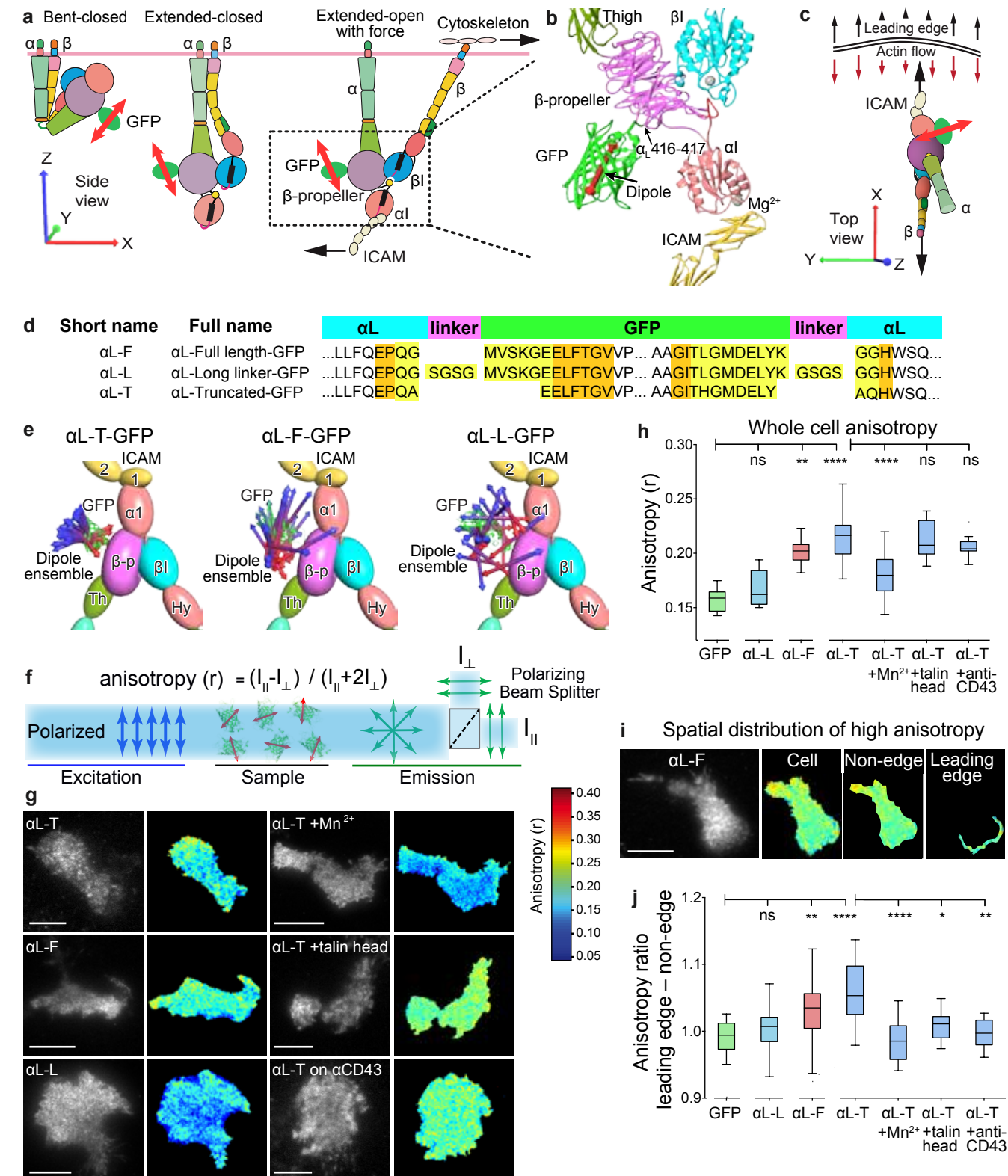


Figure 2

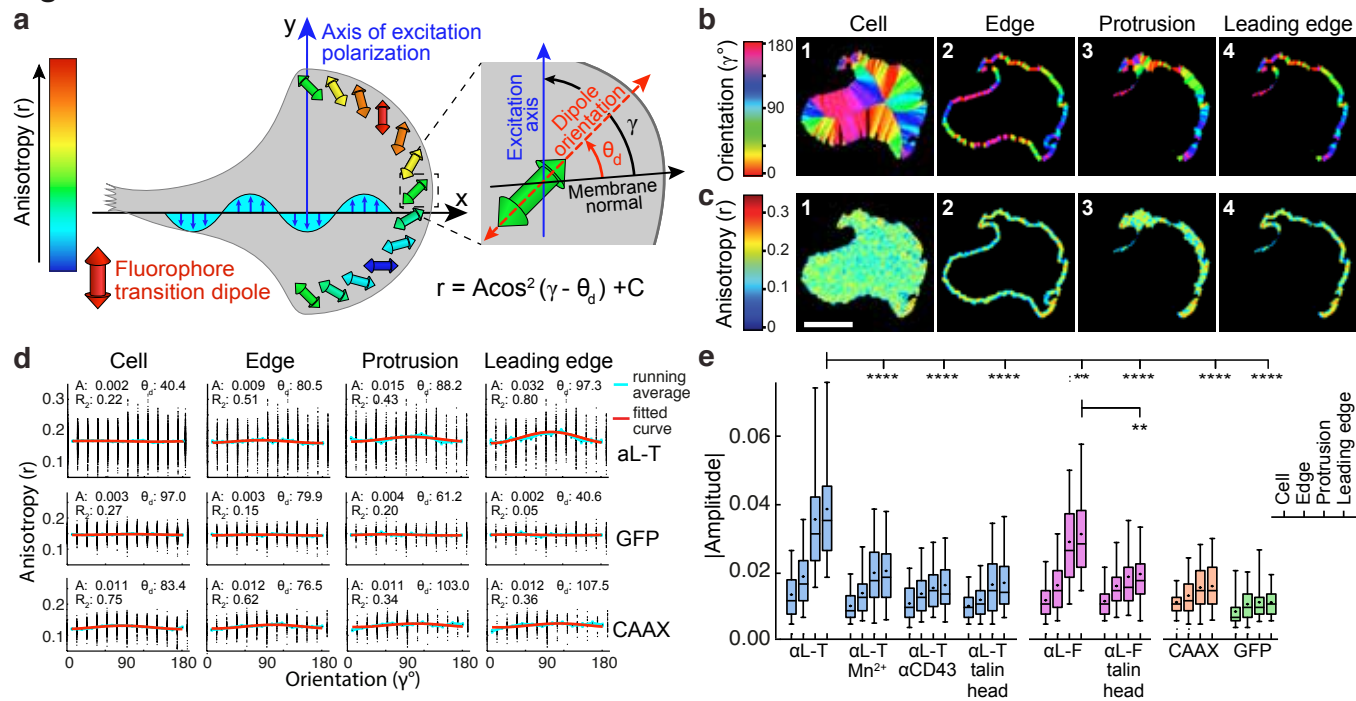


Figure 3

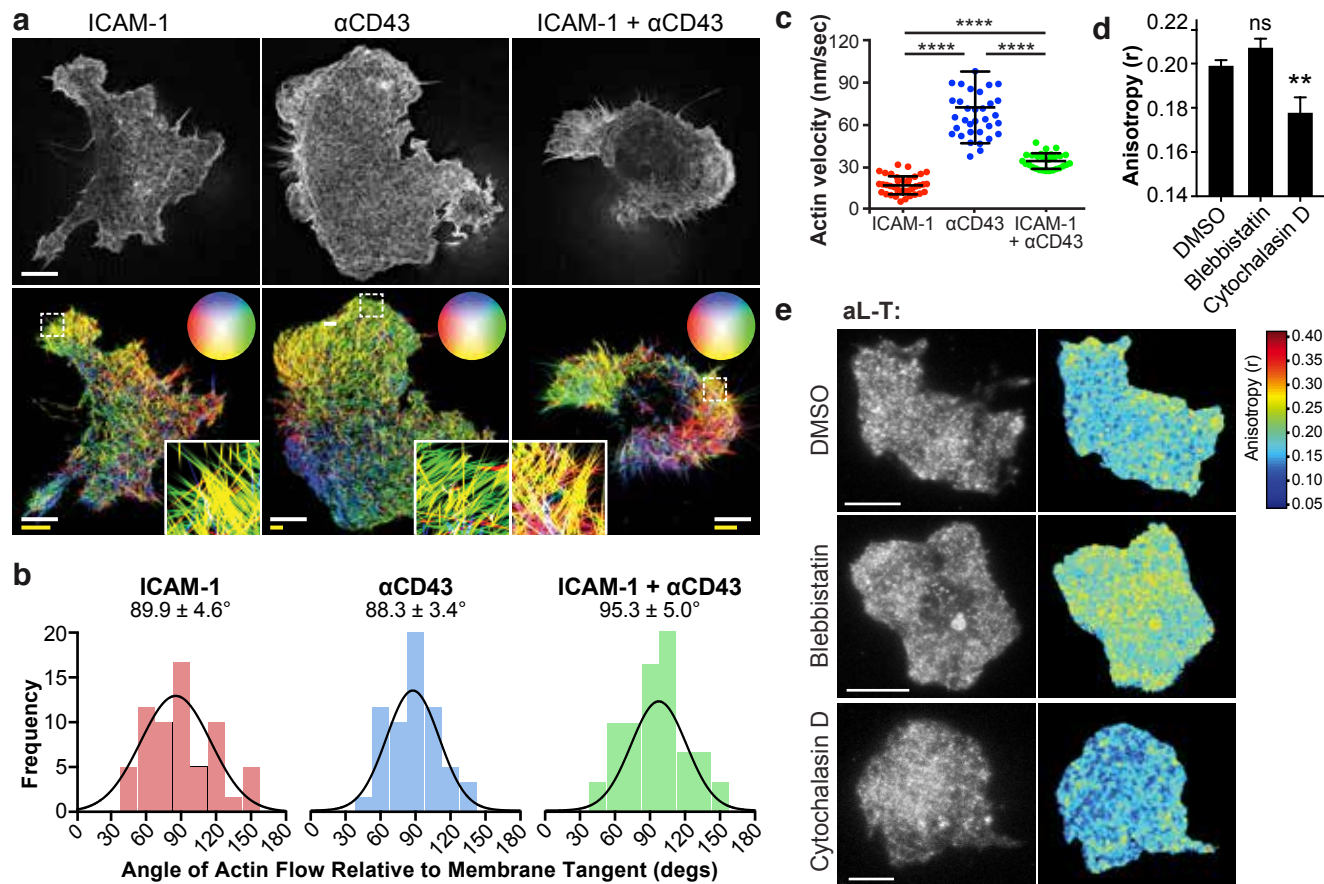


Figure 4

